Morphology Matters: 0D/2D WO₃ Nanoparticle-Ruthenium Oxide Nanosheet Composites for Enhanced Photocatalytic Oxygen Evolution Reaction Rates

Hugo A. Vignolo-González, Andreas Gouder, Sourav Laha, Viola Duppel, Sol Carretero-Palacios, Alberto Jiménez-Solano, Takayoshi Oshima, Peter Schützendübe, and Bettina V. Lotsch*

In the field of artificial photosynthesis with semiconductor light harvesters, the default cocatalyst morphologies are isotropic, 0D nanoparticles. Herein, the use of highly anisotropic 2D ruthenium oxide nanosheet (RONS) cocatalysts as an approach to enhance photocatalytic oxygen evolution (OER) rates on commercial WO₃ nanoparticles (0D light harvester) is presented. At optimal cocatalyst loadings and identical photocatalysis conditions, WO₃ impregnated with RONS (RONS/WO₃) shows a fivefold increase in normalized photonic efficiency compared to when it is impregnated with conventional ruthenium oxide (rutile) nanoparticles (RONP/WO₃). The superior RONS/WO₃ performance is attributed to two special properties of the RONS: i) lower electrochemical water oxidation overpotential for RONS featuring highly active edge sites, and ii) decreased parasitic light absorption on RONS. Evidence is presented that OER photocatalytic performance can be doubled with control of RONS edges and it is shown that compared to WO₃ impregnated with RONP, the advantageous optical properties and geometry of RONS decrease the fraction of light absorbed by the cocatalyst, thus reducing the parasitic light absorption on the RONS/WO₃ composite. Therefore, the results presented in the current study are expected to promote engineering of cocatalyst morphology as a complementary concept to optimize light harvester-cocatalyst composites for enhanced photocatalytic efficiency.

1. Introduction

Artificial photosynthesis has grown in the last decades due to its potential to store solar energy on large scale and long term by producing clean chemical fuels, such as hydrogen, with the energy input of sunlight.[1–3] Conversion of water into H₂ and O₂ utilizing sunlight is one of the most challenging yet rewarding photosynthetic processes, which is generally known as photocatalytic overall water splitting (POWS).[3–6] Water splitting is a thermodynamically uphill chemical reaction composed of simultaneous hydrogen evolution and oxygen evolution reactions (HER and OER). The OER is kinetically slower since it requires 4-electron transfer to oxidize water, and therefore, water oxidation is consistently referred to as the main kinetic bottleneck of water splitting.[2,7–10] When studying OER half-reactions, only a handful inorganic photocatalysts can harvest light efficiently, generate sufficiently oxidative holes, and

H. A. Vignolo-González, A. Gouder, S. Laha, V. Duppel,
A. Jiménez-Solano, T. Oshima, B. V. Lotsch
Max Planck Institute for Solid State Research
Heisenbergstr. 1, 70569 Stuttgart, Germany
E-mail: b.lotsch@fkf.mpg.de

H. A. Vignolo-González, A. Gouder, B. V. Lotsch
Department of Chemistry
University of Munich
LMU, Butenandtstr. 5–13, 81377 Munich, Germany

H. A. Vignolo-González, A. Gouder, B. V. Lotsch
Cluster of excellence e-conversion
Lichtenbergstr. 4a, 85748 Garching, Germany

S. Laha
Department of Chemistry
National Institute of Technology Durgapur
Mahatma Gandhi Avenue, Durgapur, West Bengal 713209, India

S. Carretero-Palacios
Departamento de Física de Materiales
Instituto de Materiales Nicolás Cabrera
Universidad
Autónoma de Madrid, Madrid 28049, Spain

A. Jiménez-Solano
Departamento de Física
Universidad de Córdoba
Campus de Rabanales, Edif. Einstein (C2), Córdoba 14071, Spain

P. Schützendübe
Physical Intelligence Department
Max Planck Institute for Intelligent Systems
Heisenbergstr. 3, 70569 Stuttgart, Germany

**ADVANCED
SCIENCE NEWS**

www.advancedsciencenews.com

**ADVANCED
ENERGY
MATERIALS**

www.advenergymat.de

catalyze water oxidation without a dedicated cocatalyst, all on the same material, that is, $BiVO_4$, Ta_3N_5, and rutile-TiO_2.[11–15] For most semiconductor light harvesters though, the addition of a cocatalyst that reduces the electrochemical overpotential for water oxidation is imperative to overcome kinetically sluggish hole-transfer at the light harvester surface. Reducing the overpotential for water oxidation at the expense of requiring an additional hole-transfer step at the light harvester/cocatalyst junction can be a beneficial compromise, if other aspects of the created interface are properly controlled (i.e., band alignment) or even improved, for example, by reducing electron–hole recombination losses through improved charge carrier separation at the new interface.[16–18] Common OER light harvesters include TiO_2 (UV), TaON, and WO_3;[13,19–22] and the most efficient OER cocatalysts are noble metal oxides, like RuO_x and IrO_x.[11,13,21,23] Optimization of the cocatalyst component of these hybrid photocatalytic systems is crucial to improve photocatalytic OER performance. In addition to cocatalyst load, close attention should be paid to tuning the deposition method, cocatalyst structure (e.g., core-shell structure), and chemical composition.[14,24,25] Such features, among others, have a direct impact on optical and photocatalytic properties of the light harvester/cocatalyst junction which ultimately govern activity, for example light absorption and charge transfer.[5,11,26,27] It is well established in literature that impregnation-calcination, photo-deposition, and hydrothermal methods can readily load active cocatalyst nanoparticles (0D morphology) directly on the surface of a semiconductor light harvester from precursor salts like $RuCl_3$, $IrCl_3$, and H_2PtCl_6.[21,23,28,29] However, despite their simplicity, reproducibility, and high degree of cocatalyst dispersion on a light harvester support, these methods generally suffer from the lack of control of cocatalyst morphology, and particle size uniformity.[11,26,30] Cocatalyst loading relates to reaction active sites. Yet, excessive loading typically results in aggregation of the cocatalyst and excessive coverage of the semiconductor, which slows down the surface redox reactions due to inaccessible active sites and hinders light absorption on the semiconductor.[11,31] A moderately better trade-off in terms of 0D cocatalyst uniformity and dispersion on the support can be achieved with the use of colloidal impregnation of previously synthesized nanoparticles (NPs) or nanoclusters instead of precursor salts.[30,32–35]

Alternatively, 1D (i.e., nanotubes) and 2D (i.e., nanosheets) materials put forward an intriguing assortment of new functionalities if used as water oxidation cocatalysts in photocatalysis, like enhanced conductivity and charge storage capacity.[36–38] Among other types of 2D inorganic structures, ruthenium oxide nanosheets (RONSs) appear especially attractive—not only promoting rapid transfer of photogenerated charge carriers across the cocatalyst/light harvester interface, but also enhancing electrocatalytic water oxidation.[39,40] Lee and co-workers used RONS as a matrix together with inorganic photocatalysts, and observed activity increase due to the rapid charge transfer from the photocatalyst to the RONS interfaces.[40]

Our group also recently reported excellent performance of RONS as an electrochemical water oxidation catalyst.[39,40] The lower overpotential for electrocatalytic water oxidation attributed theoretically to the RONS edges is desired to utilize transferred photo-generated holes more efficiently. It has also

been reported that RONS is more optically transparent compared to rutile ruthenium oxide nanoparticles (RONP).[37,41] This is advantageous to control the prevalent problem of light shielding that the latter produces on a particular light harvester support (parasitic light absorption).[11,31,34] Light absorption on the cocatalyst of a hybrid photocatalyst is often referred to in the literature as light shielding.[11,31,34,42] Out of the total light absorbed by a photocatalyst composite, in the absence of sensitization effects (i.e., plasmonics), only the fraction absorbed by the light harvester generates photocurrents. Therefore, in artificial photosynthesis, light absorption on conventional cocatalysts like RuO_x at wavelengths below the light harvester optical band gap is considered parasitic.[11,31,42,43] Although parasitic light absorption has not been formally addressed in any artificial photosynthesis performance indicator in literature to date, it is important because it relates directly to the photocatalyst solar-to-chemical efficiency.[21,44–48] Therefore, to improve the efficiency of a hybrid photocatalyst, parasitic light absorption losses should be controlled, for example, by the usage of more optically transparent cocatalyst materials like RONS.[37,41,42] The usage of 2D cocatalysts is, in any case, an emerging trend in other areas of photocatalysis. Their screening for example in HER applications evidences that 2D cocatalysts on light harvester composites produce higher rates compared to conventional 0D cocatalysts.[40,49–51]

This article highlights the combination of a 0D light harvester (commercial WO_3) and 2D (RONS) water oxidation cocatalyst (0D/2D) as a more efficient composite OER photocatalyst (RONS/WO_3) compared to its 0D/0D (RONP/WO_3) morphology equivalent (depicted in **Figure 1**). We explain the observed higher photocatalytic OER rates on RONS/WO_3 compared to RONP/WO_3, decoupling the effects of two main observations: First, taking into account the chemically distinct nature of RONS and RONP, we investigate the influence of the high electrocatalytic activity at the RONS' edge sites, evidenced by higher photocatalytic activity of samples with RONS having smaller lateral size.[39] Second, we study the influence of advantageous optical properties, arising from the 0D/2D composite morphology on photocatalysis, which we quantify as reduced (parasitic) light absorption on RONS.

2. Results and Discussion

2.1. Structure, Morphology, and Optical Properties

2.1.1. RONS

The nanosheets were prepared by exfoliation of proton exchanged $NaRuO_2$, which was synthesized as described in the literature.[39,52] The resulting $H_xNa_yRuO_2 \cdot zH_2O$ (proton exchanged $NaRuO_2$) was suspended in ultrapure water (1 mg mL^{-1}) and tetrabutylammonium hydroxide (TBAOH, 2.5 mM) to obtain suspended unilamellar RONS (see details in Experimental Section).[39] The reported exfoliation procedure has an efficiency of ≈20%, meaning the mass fraction of the initial precursor $H_xNa_yRuO_2 \cdot zH_2O$ that turns into a stable RONS colloid.[39] To make this exfoliation process more efficient, reproducible, shorter, and most importantly, to allow control of
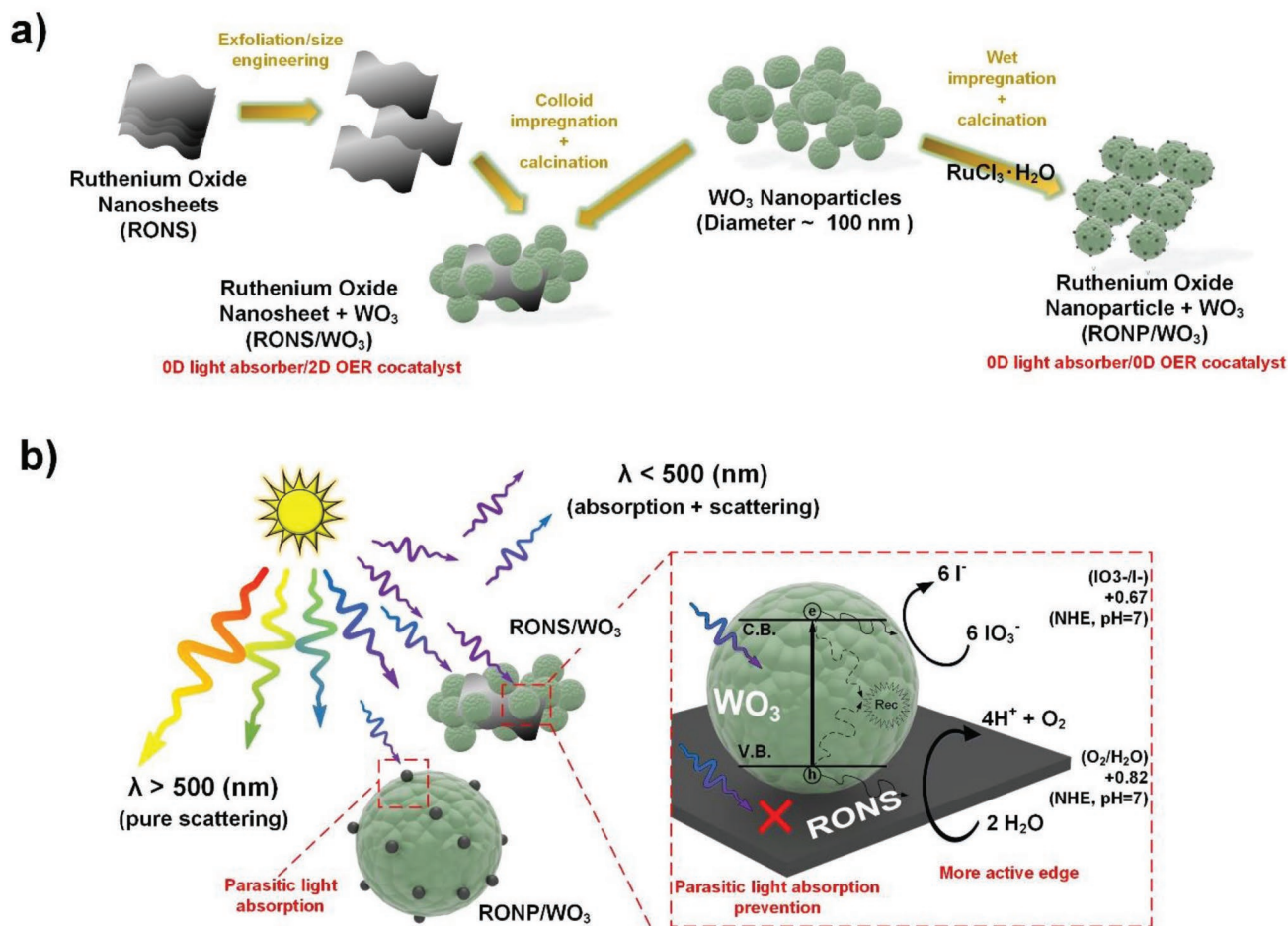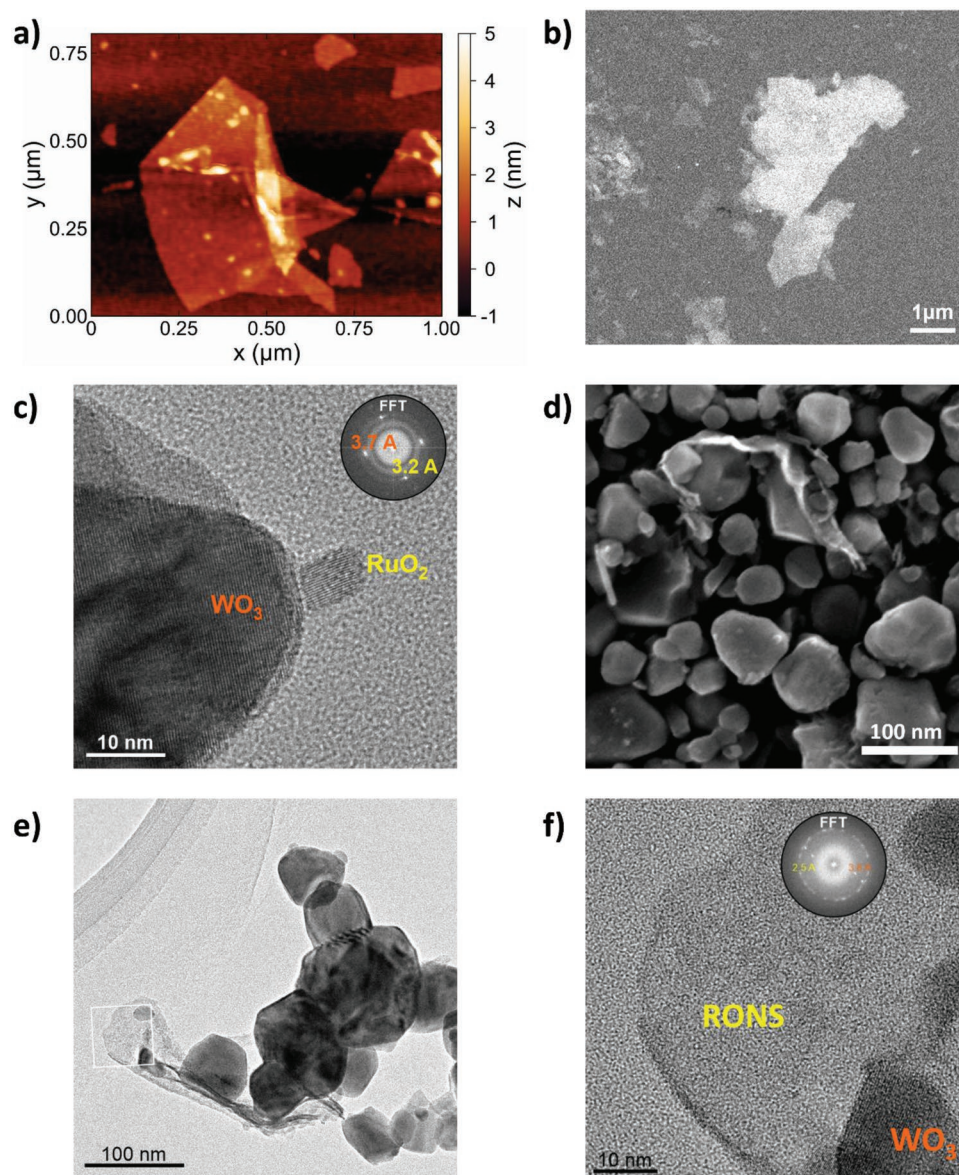
Figure 1. Schematics of 0D/2D and 0D/0D morphologies for light harvester/cocatalyst composites. a) Synthesis procedure of 0D/2D and conventional 0D/0D hybrid heterostructures. b) Advantages of photocatalytic water splitting using a WO$_3$ nanoparticle on ruthenium oxide nanosheet (RONS/WO$_3$) morphology (0D/2D) versus conventional (0D/0D) ruthenium oxide nanoparticle on WO$_3$ surface decoration (RONP/WO$_3$).

RONS lateral size, two other exfoliation variants were identified. One variant replaced previously reported daily cycles of shaking-ultrasonication of the colloids by timed vortexing (8 h) immediately followed by ultrasonication (1 h).[39] This method favors higher and more reproducible exfoliation efficiencies (≈40%) suitable for the extensive photocatalysis screening of this study. The second variant is similar to the first but introduced the additional removal of unexfoliated material after vortexing of the colloid (8 h) to obtain a stable colloid stock. The obtained colloid stock is split for different ultrasonication durations (0, 1, 2 and 3 h), to obtain ultrasonication-time-dependent RONS lateral size but at low exfoliation efficiency (≈5%). This method is used to explore nanosheet edge effects exclusively (see details of exfoliation in Experimental Section). Atomic force microscopy (AFM, **Figure 2**a) and scanning electron microscopy (SEM, Figure 2b) images are used to display the 2D morphology of single RONS. As previously reported, the nanosheet thickness is ≈1–2 nm, with a lateral size distribution dependent on the exfoliation procedure and roughly spanning from 100 nm to 1 µm.[39] Powder X-ray diffraction (PXRD) pattern in Figure S1, Supporting Information, reveals that bulk NaRuO$_2$ and H$_x$Na$_y$RuO$_2$·zH$_2$O have similar crystallinity to the ones of our previous work.[39]

2.1.2. RONS/WO$_3$ and RONP/WO$_3$ Composites

Among other OER light harvesters, WO$_3$ has a moderate band gap (2.75 eV), high thermal and photocorrosion stability, a highly oxidative valence band, and is commercially available. WO$_3$ has a conduction band with suitable electronic properties to reduce an IO$_3^-$ redox shuttle instead of irreversible sacrificial electron acceptors typically used in OER experiments, such as AgNO$_3$.[20,22,28,29,53] These attributes of WO$_3$ have made it a typical choice as oxygen evolution photocatalyst to achieve efficient POWS z-schemes (see summary of WO$_3$ photosynthetic applications in Table S1, Supporting Information).[13,20,29] Accordingly, WO$_3$ was chosen as light harvester for RONP and RONS in lieu of other semiconductors, used in the form of commercial nanopowders (particle size < 100 nm) to better benchmark its cocatalyst-dependent activity. The structure and morphology of commercial WO$_3$ nanopowders were characterized by PXRD, transmission electron microscopy (TEM), and SEM, and are presented in Figures S2–S10, Supporting Information. PXRD and TEM fast Fourier transform (TEM-FFT) of WO$_3$ powders show patterns and d-spacing in agreement with a monoclinic phase with space group $P2_1/n$ (d_{020} = 3.7 Å) reported in the literature

**ADVANCED
SCIENCE NEWS**

www.advancedsciencenews.com

**ADVANCED
ENERGY
MATERIALS**

www.advenergymat.de

Figure 2. Light harvester/cocatalyst composite morphologies and properties. a) AFM image (height profile in color map) and b) SEM image of exfoliated ruthenium oxide nanosheets (RONS) obtained with an energy and angle selective detector (EsB). c) TEM image of RONP/WO$_3$ sample after RuCl$_3 \cdot x$H$_2$O wet impregnation (0.4%wt Ru), showing the d-spacings obtained by FFT of the regions containing ruthenium oxide nanoparticles (RONP, d_{110} = 3.18 Å). d) SEM image of RONS/WO$_3$ sample after RONS wet impregnation (3%wt Ru), obtained with an Inlens detector. EDX analysis can be found in Figure S10, Supporting Information. e) TEM image of RONS/WO$_3$ sample after RONS wet impregnation (3%wt Ru), and f) zoom-in of the demarcated area (white square) showing the d-spacings obtained by FFT of the regions containing RONS. TEM-EDX analysis can be found in Figure S7, Supporting Information.

for this commercial form of WO$_3$ (Figure S2, Supporting Information, and Figure 2c).[54–56] Previously exfoliated RONS suspensions were used to impregnate WO$_3$ nanoparticles (RONS/WO$_3$) as a cocatalyst for OER. Impregnation of WO$_3$ by RONS was performed by mixing of the RONS colloid with an aqueous suspension of WO$_3$ at room temperature to form a homogeneous slurry. The slurry was then dried-off at 100 °C and under manual stirring, and grinded with pestle-mortar to obtain a fine-homogeneous powder. The wet WO$_3$ impregnation with RONP (RONP/WO$_3$) was performed similarly but replacing the RONS colloid with a RuCl$_3 \cdot$H$_2$O aqueous solution as the Ru precursor. RONS/WO$_3$ and RONP/WO$_3$ impregnated samples were adjusted to nominal wt% Ru/WO$_3$ loadings of 0.05, 0.1, 0.2, 0.4, 0.6, 1, 2 and 3. Finally, the obtained RONS/WO$_3$ and RONP/WO$_3$ powders were calcined at 400 °C for 1.5 h (see details of the WO$_3$ impregnation in Experimental Section, and in Figures S3 and S4, Supporting Information).

Inductively coupled plasma—optical emission spectrometry (ICP-OES) elemental analysis was performed to confirm the Ru loading of the produced RONS/WO$_3$ and RONP/WO$_3$ samples (see details of Ru loading estimations and ICP-OES analysis in Experimental Section and in Figure S4, Supporting

2203315 (4 of 11)

**ADVANCED
SCIENCE NEWS**

www.advancedsciencenews.com

**ADVANCED
ENERGY
MATERIALS**

www.advenergymat.de

Information). The relative error between nominal and ICP-OES measured Ru loadings of RONS/WO$_3$ and RONP/WO$_3$ samples is on average 7% and 6%, respectively. Therefore, unless stated otherwise, the nominal amount is used to refer to the Ru loadings of RONS/WO$_3$ and RONP/WO$_3$ samples. Energy dispersive X-ray spectroscopy with SEM (SEM-EDX elemental maps) and TEM (TEM-EDX) were performed to characterize RONS/WO$_3$ and RONP/WO$_3$ morphology, structure, and cocatalyst dispersion. SEM-EDX and TEM-EDX analyses in Figures S5–S10, Supporting Information, reveal that both decorated cocatalyst compositions contain Ru. As shown in Figure 2c, the decorated cocatalyst nanoparticle size of the RONP/WO$_3$ sample is ≈10 nm, with a d-spacing (3.2 Å) corresponding to that of anhydrous RuO$_2$ rutile (d_{110} = 3.17 Å), which is consistent with the literature.[21,57] At high cocatalyst loadings on WO$_3$ (3 %wt Ru), RONP has the same d-spacing, but with some portion increasing in particle size, isotropically or as short nanorods (Figures S5 and S6, Supporting Information). SEM images of RONS/WO$_3$ samples like in Figure 2d reveal an apparently less uniform cocatalyst distribution compared to RONP/WO$_3$ samples, with a nanosheet morphology akin to pure RONS in Figure 2a,b. Although the detection of RONS with SEM-EDX and TEM-EDX elemental maps is technically difficult (i.e., due to the low RONS thickness) at low magnifications (Figure S9, Supporting Information), nanosheets identified by imaging were confirmed by TEM-EDX and SEM-EDX local analysis and X-ray photoelectron spectroscopy (XPS). In RONS/WO$_3$, the increased thickness (≈10 nm) of certain spots containing RONS indicate its partial restacking during the colloid impregnation (Figure S8, Supporting Information), which partially supports the RONS' lack of uniformity on WO$_3$. RONS colloids are stable during the WO$_3$ impregnation due to the presence of TBAOH, but partial RONS restacking instead of association with WO$_3$ NPs is still expected toward the dry-off step. This competition between WO$_3$ NPs adsorption on RONS and RONS restacking occurs because the surfaces of both RONS and WO$_3$ are anionic, which was confirmed by the zeta-potential measurements in Figure S11a, Supporting Information (at pH = 7, –49 mV for RONS, and 58 mV for WO$_3$).[37,58,59] Therefore, the self-assembly of the 0D/2D structure (depicted in Figure 1) from these surfaces with the same charge relies on adhesion phenomena toward the dry-off step, and weak attractive electrostatic interactions between the surfaces of WO$_3$ and RONS in colloidal suspension, the latter mediated for example by counter ions.[60–62] These pathways for the self-assembly of iso-charged surfaces have been reported in the literature for similarly synthesized RONS and other 2D composites.[37,60–63] Dynamic light scattering observations in Figure S11b, Supporting Information, suggest an additive model for adsorption of WO$_3$ NP on RONS, which supports the idea that the aforesaid interactions between the WO$_3$ and RONS surfaces are effective for self-assembly.[59,64] Self-assembly is further supported by multiple SEM images and SEM-EDX analysis of bulk powders of RONS/WO$_3$ samples (Figures S8 and S10, Supporting Information). The latter systematically shows that RONS (or restacked RONS) were always found to be surrounded by WO$_3$ (single NP or aggregates) after calcination. Additional insights into the RONS/WO$_3$ morphology were obtained by TEM and TEM-EDX (Figure S7, Supporting Information), which confirm the 0D/2D morphology.

This morphology, regardless of partial restacking of RONS, resembles the target of 0D/2D morphology with a hybridized RONS/WO$_3$ interface similar to that depicted in Figure 1. Furthermore, SEM-EDX and TEM-EDX qualitatively confirmed the relative Ru content of different RONS-like structures as shown in Figure 2d,e (and Figures S7 and S10, Supporting Information), which points to RONS layers surrounded by WO$_3$ NP. This morphology is similar to a previously reported 0D light harvester/RONS hybrid junction, proven to be photocatalytically active.[40] The as-obtained 0D/2D morphology of the WO$_3$ NP-RONS composite has to the best of our knowledge not been used in artificial photosynthesis until now.

XPS was performed on RONS/WO$_3$ and RONP/WO$_3$ samples to check for the Ru oxidation state of RONP and RONS after impregnation, which is presented in Figure S12, Supporting Information (Ru 3d$_{5/2}$ signal). XPS analysis reveals that after the calcination, the RONP/WO$_3$ Ru 3d$_{5/2}$ signal is centered at 280.5 eV, which corresponds to anhydrous RuO$_2$ (Figure S12, Supporting Information),[19,21,29] whereas the RONS/WO$_3$ Ru 3d$_{5/2}$ signal that is centered at 280.7 eV (Figure S12, Supporting Information) is a superposition of Ru(III) and Ru(IV) peaks (RuOOH$_x$, $0 < x < 1$).[39,65] WO$_3$ background together with the low amount of RONS in the RONS/WO$_3$ sample (3 %wt Ru), make it difficult to resolve this broad and low intensity signal to individual peaks. These Ru(III) and Ru(IV) individual peaks are still visible in XPS of pure exfoliated RONS and correspond to the Ru 3d$_{5/2}$ signals as previously reported for RONS (Figure S13, Supporting Information).[39,65] XPS suggests that the fundamental chemical difference between RONP and RONS is the presence of trivalent Ru together with tetravalent Ru in RONS (RuOOH$_x$, $0 < x < 1$) whereas only tetravalent Ru is present in RONP. The properties of RuOOH$_x$ are described in our previous work (more catalytically active edge of the (110) facet).[39] Therefore, within the photocatalysis framework of this article it is considered that at equivalent Ru loading, RONS/WO$_3$ and RONP/WO$_3$ are mainly different in cocatalyst uniformity on WO$_3$, morphology, and differences in composition and edge properties of RONS and RONP, as discussed above. Multiple consequences in optics, electronics, and photocatalytic aspects can result from such differences, for example different photogenerated charge migration trends at the junction of RONS/WO$_3$ and RONP/WO$_3$. Among all those we find that two properties of RONS/WO$_3$ and RONP/WO$_3$ are significantly different, namely reduced parasitic light absorption and water oxidation overpotential in RONS/WO$_3$.

2.1.3. Optical Properties of RONS/WO$_3$ and RONP/WO$_3$

Knowledge of the optical properties of RONS and RONP is crucial to quantify differences in parasitic light absorption in a photocatalysis environment. Ruthenium oxide materials like RONS and RONP typically exhibit black color and a narrow optical band gap (<0.5 eV).[37,66–68] Diffuse reflectance UV–vis spectra of bare and impregnated WO$_3$ powders are shown in Figure S14, Supporting Information, which shows the WO$_3$ optical band gap (2.75 eV in Tauc plot), and qualitatively no evident change of absorption band edges of the composites due to RONP or RONS impregnation. The latter confirms

that RONP and RONS have optical band gaps in the IR range. The resulting broad absorption of ruthenium oxide between 450–800 nm is less for RONS/WO$_3$ than for RONP/WO$_3$, both having equal cocatalyst loading (3 %wt Ru). This difference is also evident to the bare eye (Figure S14, Supporting Information). To properly quantify such observations suggesting that parasitic light absorption in RONS/WO$_3$ is less pronounced than for RONP/WO$_3$, UV–vis diffuse reflectance and transmittance ($T + R$) was measured on suspensions of both samples at equivalent Ru content (nominal %wt Ru), at each of the Ru loading levels used for the WO$_3$ impregnation with cocatalyst (see depiction of experiments in Figure S15, Supporting Information). Suspensions containing samples like in photocatalysis conditions were introduced into an integrating sphere and absorptance ($A = 1 - (R + T)$) was measured in the range of 300 to 800 nm (see details of UV–vis measurements in Experimental Section). In addition to the absorptance of RONS/WO$_3$ and RONP/WO$_3$ photocatalysis samples (Figures S16a and S17b, Supporting Information), the absorptance of pure RONS colloidal suspensions was measured (Figure S16b,c, Supporting Information). The mass of Ru contained in the pure RONS colloids is equivalent to the one of RONS/WO$_3$ composites at each Ru loading level (%wt Ru). The WO$_3$ background used for absorptance correction can be found in Figure S17a, Supporting Information, for different suspension densities. Above the absorption range of WO$_3$ ($\lambda > 450$ nm) and at equivalent Ru mass in suspension, for example at 2 %wt Ru, pure RONS absorbs roughly 45% less light than RONP/WO$_3$ (in Figure S16b, Supporting Information, average of the 500–800 nm wavelength range). Although this is in line with the previously reported high optical transparency of RONS, below 600 nm the pure RONS absorptance increases and begins to approach the one of RONP/WO$_3$ at equivalent Ru mass in suspension.[37,41] When comparing pure RONS versus RONS/WO$_3$ at equivalent Ru mass in suspension in the same wavelength range, the average light absorption on WO$_3$-supported RONS is reduced by ≈30–40% at loadings > 0.6 %wt Ru (Figure S16c, Supporting Information). In this wavelength range (500–800 nm), such decrease in cocatalyst light absorption can be explained by the scattering of photons reaching the surrounding WO$_3$ nanoparticles of the RONS/WO$_3$ composite. In absorptance measurements, this event favors ultimately photon scattering out of the suspension over absorption on the exposed surface of RONS. For every wavelength and at equivalent cocatalyst load, RONS/WO$_3$ samples present always the lowest cocatalyst light absorption when compared to pure RONS or RONP/WO$_3$ (Figure S16, Supporting Information). This is a convolution of geometrical aspects (cocatalyst exposure), cocatalyst transparency (i.e., due to chemical and geometrical differences compared to RONP), and the fate of photons impinging on the WO$_3$ part of the composites.

To deconvolute these different contributions to the decreased cocatalyst light absorption of the RONS/WO$_3$ samples, we model light interaction with the photocatalyst components considering two possible scenarios (see details of optical modeling in Experimental Section). In a first scenario, we explain the lower cocatalyst light absorption of pure RONS versus RONP/WO$_3$ (Figure S16b, Supporting Information). For such, we model the photons that impinge on exposed RONS and RONP to study the influence of RONS morphology and optical properties on cocatalyst light absorption. In a second scenario, we explain the lower cocatalyst light absorption of pure RONS versus RONS/WO$_3$ (Figure S16c, Supporting Information). For such, we model the photons that impinge on WO$_3$ to study the influence of lower RONS exposure to photons on cocatalyst light absorption. The modeled scenarios rationalize UV–vis experimental observations and suggest that the RONS high transparency and optically shielded RONS (by WO$_3$ NPs) may effectively control parasitic light absorption on the RONS/WO$_3$ samples during photocatalysis (see optical modeling analysis in Supporting Information, and in Figures S18–S20, Supporting Information).

The optics quantitative analysis presented hitherto considers a wavelength range where WO$_3$ only scatters photons (500–800 nm), because we cannot directly access the fraction of light that is parasitically absorbed in RONS/WO$_3$ and RONP/WO$_3$ samples when WO$_3$ also absorbs light. On the one hand, it can be assumed that the lower cocatalyst light absorption of RONS/WO$_3$ at wavelengths above 500 nm may result in less optical losses during photocatalysis (see optical modeling analysis in Supporting Information). On the other hand, light absorption on WO$_3$ is the utmost requirement for photocatalysis, hence parasitic light absorption is only relevant if estimated for wavelengths below 500 nm. In later sections, we derive from the aforesaid quantitative observations at wavelengths between 500 and 800 nm an upper limit of parasitic light absorption for the relevant photons (400 to 500 nm) irradiated on RONS/WO$_3$ and RONP/WO$_3$ suspensions.

2.2. Photocatalytic Properties of RONS/WO$_3$ and RONP/WO$_3$

It is well documented that the ruthenium oxide/WO$_3$ heterojunction favors charge separation in WO$_3$ and lowers the overpotential of water oxidation.[11,31,69] However, if ruthenium oxide loading is too high, further increase of OER rates is limited by parasitic light absorption and increased surface recombination at the ruthenium oxide centers, and shields WO$_3$ active sites.[11,31,69] Previously described optical and photocatalytic differences of RONS and RONP are key to explain dissimilar OER rates after the WO$_3$ impregnation, and why their optimal ruthenium oxide loadings on WO$_3$ differs. It must be noted that the less uniform cocatalyst distribution of RONS/WO$_3$ compared to the highly dispersed RONP/WO$_3$ may also play a role in photocatalytic activity, as well as additional electrochemical cocatalyst differences.[38,52] These additional differences are not considered quantitatively in the OER photocatalytic rate analysis presented in this section, in view of the larger impact expected from the well-established lower water oxidation overpotential of RONS compared to RONP as discussed below, and the suppressed parasitic light absorption of the RONS.[38,39,52,70,71]

2.2.1. Photocatalytic OER Rates and Cocatalyst Performance on WO$_3$

To probe the immediate influence of optics and electrochemical properties on the photocatalytic properties in water oxidation,
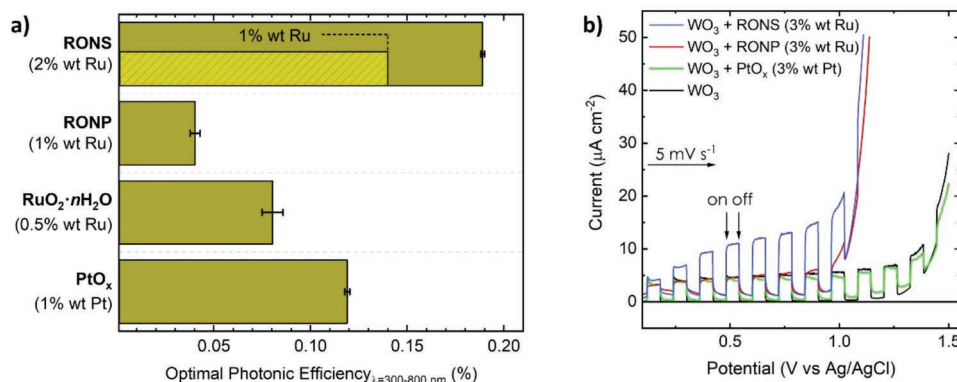
Figure 3. Activity benchmark of different cocatalysts on WO_3. a) Comparison of photocatalytic OER activity of different cocatalysts optimally loaded on WO_3, using the concept of optimal photonic efficiency (ξ_e). Inset within the RONS bar shows activity of the RONS loaded on WO_3 at 1 %wt Ru. Photocatalysis conditions: 10 mL ultrapure water, 10 mM KIO_3, 0.5 mg mL^{-1} of sample and attenuated solar spectra (Figure S24, Supporting Information, 65 mW cm^{-2}). Error bars represent mean ± standard error of the mean of the average activity of two independent batches of sample (see details in Experimental Section). Optimal photonic efficiency of RuO_2/TiO_2 benchmark for rate standardization is 0.27% (relative optimal photonic efficiency, ξ'_e). ξ'_e of WO_3 impregnated with optimal cocatalyst loadings of RONS (2 %wt Ru), RONP (1 %wt Ru), PtO_x (1 %wt Pt) and $RuO_2 \cdot nH_2O$ (0.5 %wt Ru) are, respectively, 0.80, 0.15, 0.48 and 0.32. b) LSV profiles for WO_3 + cocatalyst electrodes in 0.1 M aqueous Na_2SO_4 solution, and curves under chopped AM 1.5 G irradiation (dashed-dot lines). Scan rate: 5 mV s^{-1}

$RONP/WO_3$ and $RONS/WO_3$ were tested for photocatalytic OER activity. Photocatalysis was performed in a water suspension (ultrapure water, 0.5 mg mL^{-1}) under attenuated simulated sunlight (65 mW cm^{-2}) and using KIO_3 as electron acceptor (10 mM). OER rates were measured in a continuous photocatalytic high throughput cell described in our previous work.[21] The maximum OER rate in time was recorded for both samples at different loadings, and at plateau of photonic efficiency versus suspension volume (optimal photonic efficiency, ξ_e), which is shown in **Figure 3**a.[21,45] At loadings of 1 %wt Ru/WO_3 for both RONS and RONP, which is optimal only for RONP, the $RONS/WO_3$ sample shows a 3.5-fold increase in ξ_e compared to $RONP/WO_3$ (0.13% and 0.038%, respectively). Upon the impregnation of WO_3 with additional RONS, the resulting optimally loaded $RONS/WO_3$ sample (2 %wt Ru/WO_3) shows a fivefold increase in ξ_e (0.19%) compared to the optimally loaded $RONP/WO_3$. This optimal ξ_e of the $RONS/WO_3$ sample remained constant at a higher RONS loading of 3 %wt Ru/WO_3. The fact that the photocatalytic activity of RONS plateaus at Ru loadings on WO_3 up to three times higher than optimally loaded $RONP/WO_3$ is explained later based on the RONS optical properties.

The dynamic OER rate measurement of $RONS/WO_3$ can be found in a long illumination test in Figure S21, Supporting Information, which shows that $RONS/WO_3$ is stable under photocatalysis conditions (7 h). No signs of deactivation were observed on $RONP/WO_3$ either after long illumination times. Under the same conditions, bare WO_3 has no activity above our detection limits, and ξ_e of a RuO_2/TiO_2 benchmark (AM 1.5G, 300–800 nm) for rate standardization is 0.27% ± 0.05% (relative optimal photonic efficiency, ξ'_e). Optimal photonic efficiencies ξ_e in Figure 3a are reported using good practices for measuring OER rates (see Supporting Information for details).[21,45,46,72] These practices include normalization of OER rates, minimization of artificial O_2 rates from electron acceptor decomposition, and ^{18}O labeling experiments (Figure S22 and Table S2, Supporting Information). Normalized activities of $RONP/WO_3$

($\xi_e = 0.15$) and $RONS/WO_3$ ($\xi_e = 0.8$) in Figure 3a were later refined with photocatalytic OER measurements in a second reactor cell with more controlled optics (see Supporting Information for details). To fully assess standardized performance indicators, photonic efficiency and apparent quantum yield (AQY) results obtained in this alternative cell for $RONP/WO_3$ and $RONS/WO_3$ OER are presented in Figure S23a,b, Supporting Information, respectively (lamp spectra in Figure S24, Supporting Information).

In Figure 3a, it is shown that ξ'_e of $RONS/WO_3$ even surpasses the one of WO_3 impregnated at optimal loadings of PtO_x ($\xi'_e = 0.47$, 1 %wt Pt) and $RuO_2 \cdot nH_2O$ ($\xi'_e = 0.32$, 0.5–1 %wt Ru); details of PtO_x and $RuO_2 \cdot nH_2O$ can be found in the Experimental Section. PtO_x and $RuO_2 \cdot nH_2O$ are the most active inorganic 0D cocatalysts on WO_3 reported to date for photocatalytic OER using IO_3^- as an electron acceptor.[19,20,28,29] However, both PtO_x and $RuO_2 \cdot nH_2O$ are inherently different cocatalysts. They are benchmarked on WO_3, but they should not be compared directly with RONP (or RONS). While anhydrous RuO_2 (RONP) is a well-established water oxidation electrocatalyst with moderate additional activity for IO_3^- reduction, PtO_x and $RuO_2 \cdot nH_2O$ are primarily cocatalysts for reduction of IO_3^-.[19,20,28,29] Even so, RONP and other RuO_x species are considered bifunctional cocatalysts that promote, to different extents, both water oxidation and IO_3^- reduction.[19,20,29] To rule out that higher OER rates on $RONS/WO_3$ are just the consequence of the previously reported faster IO_3^- reduction rates on certain RuO_x catalysts, (photo)electrochemical measurements (Linear Sweep Voltammetry, LSV) were performed on WO_3, $RONS/WO_3$, $RONP/WO_3$, and PtO_x/WO_3. Dark LSV measurements show that RONS (and RONP) electrocatalytic activity relates mostly to water oxidation, being the RONS the electrocatalyst with the lowest IO_3^- reduction and the highest water oxidation activity (Figure S25a,b, Supporting Information). Under chopped illumination (Figure 3b), $RONS/WO_3$ also exhibits the highest water oxidation photocurrent (10 µA cm^{-2} at a potential of 0.5 V vs Ag/AgCl). These observations denote

that higher photocatalytic OER rates of RONS/WO₃ versus RONP/WO₃ are unequivocally related to the beneficial optical properties of RONS/WO₃, and the higher water oxidation electrocatalytic activity of the RONS (see details of the electrochemistry and photoelectrochemistry analysis in Supporting Information). In the next sections, these two features of RONS/WO₃ are discussed in the context of photocatalysis.

2.2.2. Lower Water Oxidation Overpotential of RONS edges

The first key aspect for the higher photocatalytic OER activities of RONS/WO₃ is the higher electrocatalytic activity of the RONS edges when compared to anhydrous RuO₂ (0.76 V lower overpotential for water oxidation).[39] It is expected in WO₃ photocatalysis that this "electrocatalytic advantage" of RONS over RONP facilitates a more efficient extraction of the photogenerated holes reaching the cocatalyst/WO₃ interface; assuming that water oxidation controls hole extraction rates.[11,31,73,74] Higher cocatalyst electrocatalytic activity simultaneously reduces accumulation of photogenerated holes at the cocatalyst/WO₃ interface, which indirectly reduces charge recombination in WO₃.[73–75] Altogether, the more active RONS edge is then necessary to rationalize the higher RONS/WO₃ photocatalytic OER rates.

To prove this effect in photocatalysis, RONS colloids displaying controlled nanosheet lateral sizes were impregnated at equal loading on WO₃. Nanosheets with different lateral sizes were obtained by varying the ultrasonication time of a unique RONS colloid stock, which was previously prepared by vortexing/centrifugation. Subsequent ultrasonication of the stock decreases the sheets' lateral dimension, which increases the edge-to-volume ratio of RONS that we have linked to its higher cocatalyst water oxidation activity (see details of RONS exfoliation in Experimental Section). We measured photocatalytic OER rates of RONS/WO₃ samples impregnated with such RONS colloid stock (at 20 and 50 mM TBAOH), at equal cocatalyst loading (≈0.25 %wt Ru, Figure S26, Supporting Information), but different ultrasonication duration before WO₃ impregnation. Results showing the OER rate differences with ultrasonication times are presented in **Figure 4**a. At 20 mM TBAOH, the maximum OER activity of RONS/WO₃ was obtained for the colloid vial sonicated for 1 h (50% increase compared to no sonication). Lateral size distributions obtained from AFM images of the RONS before impregnating of WO₃ are displayed in Figure 4b for the same samples screened in Figure 4a. The most significant decrease in nanosheet lateral size occurs after 1 h of ultrasonication of the colloid stock (Figure S27, Supporting Information, and Figure 4b). The corresponding RONS/WO₃ sample shows the highest photocatalytic OER activity (Figure 4a). The optimal ultrasonication time of the RONS colloid used to produce RONS/WO₃ photocatalysis samples relates to an observed compromise between RONS lateral size and agglomeration (see details of the RONS size dependent photocatalysis studies in Supporting Information, and in Figures S27 and S28, Supporting Information). Still, our results show that the maximum activity is linked to the sharpest decrease in nanosheet lateral size, and thus that more active edge sites play a role in photocatalysis. This observation
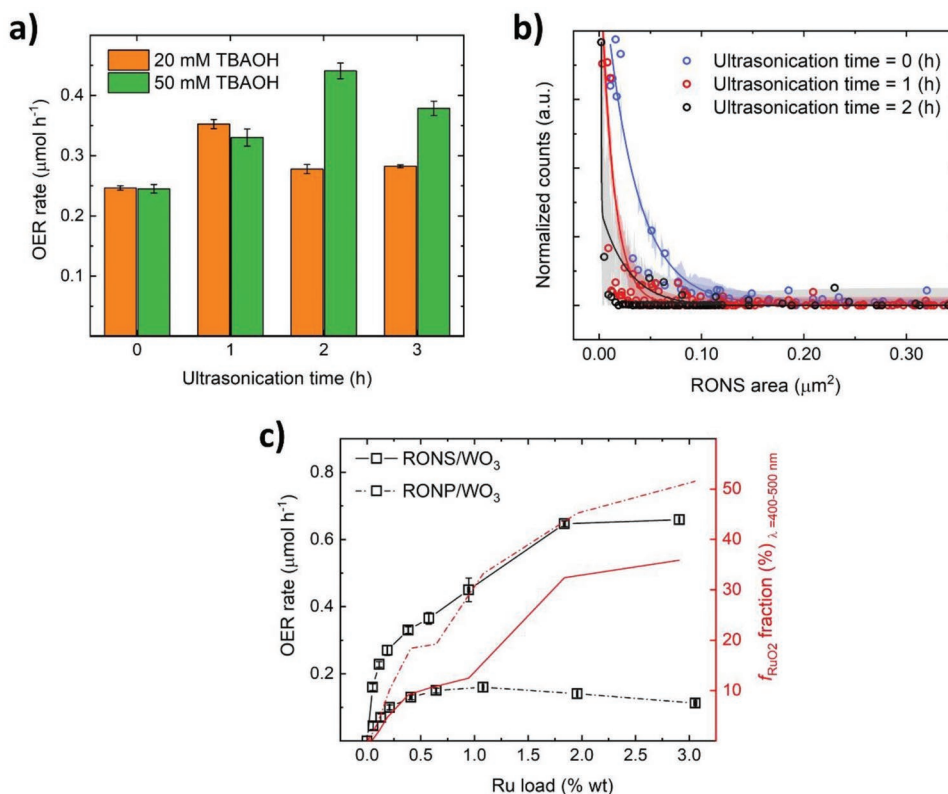
is supplemented with the second experiment at identical conditions but increasing the TBAOH concentration (50 mM) to stabilize the small agglomerates during extended ultrasonication. Accordingly, the experiment at 50 mM TBAOH shows a ≈100% increase in activity at 2 h of ultrasonication (Figure 4a) of the colloid compared to no ultrasonication. Additionally, photocatalysis experiments were performed using an OER suitable dye ([Ru(bpy)₃]²⁺ 2Cl⁻) as light harvester instead of WO₃ (and Na₂S₂O₈ as sacrificial electron acceptor),[76,77] to isolate the edge effects from other influences such as those due to RONS/WO₃ hybridization efficiency during the impregnation step (Figure S29, Supporting Information). The trend obtained is similar, presumably because agglomeration of RONS colloids during ultrasonication still reduces the surface area for hole transfer to [Ru(bpy)₃]²⁺. Dye experiments likewise show such distinctive increase of OER rates with ultrasonication time and hence confirm that more RONS edges increases photocatalytic OER rates (Figure S29c, Supporting Information).

2.2.3. Parasitic Light Absorption on RONS/WO₃ and RONP/WO₃

We quantify in this section the impact of parasitic light absorption on the superior photocatalytic performance of RONS/WO₃, by building upon the cocatalyst light absorption differences of RONP/WO₃ and RONS/WO₃ analyzed in previous sections (500–800 nm range). We have established that such trends result from multiple optical differences between RONP and RONS that arise, for example, from different electric properties. We extrapolate the experimentally measured cocatalyst absorptance (%) for each cocatalyst loading to photocatalysis conditions as an estimation of parasitic light absorption (see Experimental Section for calculations and assumptions details). This estimation sets an upper limit for the fraction of the irradiated relevant photons (400–500 nm) being absorbed by the cocatalyst during photocatalysis, which we define as the parasitic light absorption fraction (f_{RuO2}).

Figure 4c shows the trends of photocatalytic OER rates and f_{RuO2} of RONP/WO₃ and RONS/WO₃ versus different cocatalyst loadings (rates at optimal cocatalyst loading are used to calculate optimal photonic efficiencies in Figure 3a). Meaningful comparison of two photocatalyst material performances requires calculations of the internal photonic efficiency or quantum yields, and thus the quantification of suspension absorptance under photocatalysis conditions.[21,72] Given that both RONP/WO₃ and RONS/WO₃ samples have an identical WO₃ light harvester support, their photocatalytic OER rates can be compared directly since differences in light absorptance of RONP/WO₃ and RONS/WO₃ suspensions come primarily from optical losses related to f_{RuO2}. Plateauing of OER rates with cocatalyst loading for RONP/WO₃ (1 %wt Ru) and RONS/WO₃ (2 %wt Ru) occurs around $f_{RuO2} = 20$–30%. Optimal cocatalyst loading of RONP/WO₃ and RONS/WO₃ cannot be explained quantitatively based on this optical limit only. In addition to the fraction of photons effectively absorbed by WO₃, the cocatalyst effect on internal photonic efficiency is also dependent on charge carrier dynamics of photogenerated charges. OER rates at the cocatalyst/WO₃ junction depend on multiple (opto)electronic factors such as cocatalyst/WO₃ band alignment, charge separation,

ADVANCED
SCIENCE NEWS
www.advancedsciencenews.com

ADVANCED
ENERGY
MATERIALS
www.advenergymat.de

Figure 4. Influence of lower cocatalyst water oxidation overpotential and parasitic light absorption on photocatalytic OER rates. a) Comparison of photocatalytic OER rates at equal loading of RONS on WO_3 (0.25–0.33 %wt Ru, Figure S26, Supporting Information), exfoliated using only 12 h vortexing, but later ultrasonicated at different times (x-axis) before the WO_3 colloid impregnation. TBAOH concentrations during exfoliation are 20 and 50 mM. Photocatalysis conditions: 10 mL ultrapure water, 10 mM KIO_3, 0.5 mg mL^{-1} of sample and attenuated solar spectra (Figure S24, Supporting Information, 65 mW cm^{-2}). Error bars represent mean ± standard error of the mean of the average activity of two independent batches of sample (see details in Experimental Section). b) Nanosheet lateral size distribution from AFM images of the vortexed exfoliated RONS at different ultrasonication times and 20 mM TBAOH (x-axis in (a)). Solid lines correspond to the distribution fit (triple exponential, 95% confidence band in colored area). Example of surveyed AFM images, including sample after 3 h of ultrasonicated, can be found in Figure S27, Supporting Information. c) Photocatalytic OER rates versus the cocatalyst loadings impregnated on WO_3 (x-axis considers Ru loadings measured by ICP-OES elemental analysis, Figure S4c, Supporting Information). Photocatalysis conditions: 10 mL ultrapure water, 10 mM KIO_3, 0.5 mg mL^{-1} of sample and attenuated solar spectra (Figure S24, Supporting Information, 65 mW cm^{-2}). Error bars represent mean ± standard error of the mean of the average activity of two independent batches of sample (see details in Experimental Section). Secondary y-axis (red) represents the fraction of irradiated light that is parasitically absorbed by the cocatalyst (f_{RuO2}) versus cocatalyst loading, estimated from UV–vis measurements (Figures S16a and S17c, Supporting Information) and optical modeling (Figure S18c, Supporting Information), and extrapolated to the wavelength range of 400–500 nm (see Experimental Section for f_{RuO2} calculations and assumptions details).

and water oxidation overpotential of the cocatalyst.[11,16,17,31] For example, assuming a recombination-limited model mediated by hole-trapping at the surface of the semiconductor, OER rates are proportional to active sites for water oxidation.[16,73,74] In this scenario, based on mass action law, the coarse grain probability of hole transfer to ruthenium oxide depends linearly on the concentration of photogenerated holes at the WO_3 surface, and cocatalyst availability.[73,74] At the same time, OER rates must satisfy the electrochemical relation between water oxidation rates at the cocatalyst surface and the available overpotential of the surface hole.[11,31] OER rates also improve with cocatalyst addition, due to the heterojunction properties that may generate a significant upward band bending (i.e., 1.22 V for RuO_2/TiO_2).[69,78,79] This likely upward band bending at the ruthenium oxide/WO_3 junction reduces charge recombination due to electric field induced electron–hole separation.[69,78–80] Altogether, at low cocatalyst loadings and proper band alignment, OER rates

are expected to increase with cocatalyst addition. This can be seen in Figure 4c for both RONP/WO_3 and RONS/WO_3. At loadings of <0.2 wt% Ru, photocatalytic OER rates increase sharply with cocatalyst load, with little influence of adverse effects like parasitic light absorption (f_{RuO2} < 10%). On the other hand, OER rates plateau with more ruthenium oxide centers at high loads, because of multiple factors, like the increasing formation of unavailable cocatalyst active sites.[11,31,69] Excessive ruthenium oxide loading increases the nanoparticle size of RONP and likely leads to restacking of RONS. All these factors create an intricate relation between parasitic light absorption, photogenerated charge carrier dynamics, and optimal cocatalyst loading. Likewise, junction properties controlling OER rates are intrinsically different between RONP/WO_3 and RONS/WO_3.[39–41,50,52] For example, the edge of RONS has a lower water oxidation overpotential compared to rutile RuO_2, which was described formerly as another factor to explain higher OER

activities of RONS/WO$_3$.[39] Regardless of such complexities, the common parasitic light absorption threshold of 20–30% described in Figure 4c still emerges as the limiting factor for cocatalyst load in both RONP/WO$_3$ and RONS/WO$_3$. Parasitic light absorption partially explains the higher optimal cocatalyst loadings of RONS/WO$_3$. Due to the beneficial optical properties of RONS, RONS/WO$_3$ shows an evident stretch of the f_{RuO2} function versus cocatalyst loading, which also translates to less optical losses and overall higher OER rates on RONS/WO$_3$.

3. Conclusion

We have established that a 2D morphology presents evident advantages compared to conventional 0D morphologies in Ru-based cocatalysts to obtain higher photocatalytic OER on a commercial light harvester (WO$_3$). RONS impregnated on WO$_3$ (RONS/WO$_3$, 2 %wt Ru) show a fivefold increase in photonic efficiency compared to RONP impregnated on WO$_3$ (RONP/WO$_3$, 1 %wt Ru)—both at their optimal Ru loading. We have demonstrated that this increase of photocatalytic OER performance is related to more beneficial optical and electrochemical properties of RONS for water oxidation. We have quantified the former and the latter using the concepts of controlled parasitic light absorption (f_{RuO2}), and lower electrochemical overpotential for water oxidation at RONS edges, respectively. A low electrochemical overpotential at the RONS edge was previously identified under electrocatalytic water splitting conditions and assigned to higher activity of the RONS edges. We have systematically demonstrated the impact of RONS edges on photocatalytic OER rates for the first time, which we have controlled indirectly by engineering the RONS exfoliation/ aggregation state and size. In addition, we introduced and quantified the concept of the fraction of parasitic light absorption by the cocatalyst, f_{RuO2}, which is barely discussed in photocatalysis literature, and we show here that it has quantitative impact on light absorption efficiency by the light absorber. The optical properties established for RONS and the 0D/2D as compared to the conventional 0D/0D morphology allow us to rationalize the observed correlation between catalytic activity and catalyst loading, a concept that may generate particular interest in the context of earth-abundant cocatalysts for artificial photosynthesis. While we have demonstrated that 2D RONS show higher activity as OER cocatalyst than 0D RONP, we have also shown that RONS stand out in a photocatalysis benchmark against other reported 0D cocatalysts on WO$_3$, such as PtO$_x$, and RuO$_2 \cdot n$H$_2$O, under the photocatalysis conditions used in this study. Finally, we present an alternative to the regular light harvester chemical, structural, and electronic tuning by adding the concept of morphology tuning to identify more efficient composite catalyst systems for artificial photosynthesis. On the one hand, the use of 1D and 2D morphologies in semiconductor light harvesters typically exhibits beneficial properties, for example, to decrease photogenerated charge carrier recombination. This has been widely exploited in artificial photosynthesis (i.e., as 2D light harvester/0D cocatalyst). On the other hand, the use of cocatalysts with 2D morphology (rather than 0D) like RONS is an emerging trend in photocatalysis but rarely applied yet to energy conversion systems. Based on

results from related fields of study, we believe that synergies in simultaneous light harvester and cocatalyst morphology design present unique opportunities to assemble more efficient inorganic photosynthetic systems.[14,42] The results presented herein and other interesting properties of 2D materials mentioned in this article thus open multiple possibilities for cocatalyst morphology engineering.

Supporting Information

Supporting Information is available from the Wiley Online Library or from the author.

Conflict of Interest

The authors declare no conflict of interest.

Data Availability Statement

The data that support the findings of this study are available in the supplementary material of this article.

[1] T. Hisatomi, K. Domen, *Faraday Discuss.* **2017**, *198*, 11.
[2] T. Grewe, M. Meggouh, H. Tüysüz, *Chem. - Asian J.* **2016**, *11*, 22.
[3] J. H. Kim, D. Hansora, P. Sharma, J. W. Jang, J. S. Lee, *Chem. Soc. Rev.* **2019**, *48*, 1908.
[4] F. E. Osterloh, *ACS Energy Lett.* **2017**, *2*, 445.
[5] Z. Wang, C. Li, K. Domen, *Chem. Soc. Rev.* **2019**, *48*, 2109.
[6] M. A. Nadeem, M. A. Khan, A. A. Ziani, H. Idriss, *Catalysts* **2021**, *11*, 60.

[7] M. D. Kärkäs, E. V. Johnston, O. Verho, B. Akermark, *Acc. Chem. Res.* **2014**, *47*, 100.

[8] Q. Wang, K. Domen, *Chem. Rev.* **2020**, *120*, 919.

[9] H. Idriss, *Catal. Sci. Technol.* **2020**, *10*, 304.

[10] K. Sivula, *ACS Energy Lett.* **2020**, *5*, 1970.

[11] B. Mei, K. Han, G. Mul, *ACS Catal.* **2018**, *8*, 9154.

[12] A. Miyoshi, S. Nishioka, K. Maeda, *Chemistry* **2018**, *24*, 18204.

[13] S. Chen, T. Takata, K. Domen, *Nat. Rev. Mater.* **2017**, *2*, 17050.

[14] Q. Wang, T. Hisatomi, Q. Jia, H. Tokudome, M. Zhong, C. Wang, Z. Pan, T. Takata, M. Nakabayashi, N. Shibata, Y. Li, I. D. Sharp, A. Kudo, T. Yamada, K. Domen, *Nat. Mater.* **2016**, *15*, 611.

[15] Z. Wang, Y. Inoue, T. Hisatomi, R. Ishikawa, Q. Wang, T. Takata, S. Chen, N. Shibata, Y. Ikuhara, K. Domen, *Nat. Catal.* **2018**, *1*, 756.

[16] Z. Pan, R. Yanagi, Q. Wang, X. Shen, Q. Zhu, Y. Xue, J. A. Röhr, T. Hisatomi, K. Domen, S. Hu, *Energy Environ. Sci.* **2020**, *13*, 162.

[17] A. T. Garcia-Esparza, K. Takanabe, *J. Mater. Chem. A* **2016**, *4*, 2894.

[18] F. Lin, S. W. Boettcher, *Nat. Mater.* **2014**, *13*, 81.

[19] K. Maeda, K. Abe, K. Domen, *J. Phys. Chem. C* **2011**, *115*, 3057.

[20] R. Abe, M. Higashi, K. Domen, *ChemSusChem* **2011**, *4*, 154.

[21] H. A. Vignolo-González, S. Laha, A. Jiménez-Solano, T. Oshima, V. Duppel, P. Schützendübe, B. V. Lotsch, *Matter* **2020**, *3*, 464.

[22] W. Erbs, J. Desilvestro, E. Borgarello, M. Graetzel, *J. Phys. Chem.* **1984**, *88*, 4001.

[23] M. Dilla, A. Jakubowski, J. Strunk, S. Ristig, J. Strunk, R. Schlögl, *Phys. Chem. Chem. Phys.* **2019**, *21*, 15949.

[24] K. Maeda, K. Teramura, N. Saito, Y. Inoue, K. Domen, *J. Catal.* **2006**, *243*, 303.

[25] K. Maeda, K. Teramura, D. Lu, N. Saito, Y. Inoue, K. Domen, *Angew. Chem.* **2006**, *118*, 7970.

[26] K. Wenderich, G. Mul, *Chem. Rev.* **2016**, *116*, 14587.

[27] W. Wang, L. Qi, *Adv. Funct. Mater.* **2019**, *29*, 1807275.

[28] S. S. K. Ma, K. Maeda, R. Abe, K. Domen, *Energy Environ. Sci.* **2012**, *5*, 8390.

[29] H. Suzuki, S. Nitta, O. Tomita, M. Higashi, R. Abe, *ACS Catal.* **2017**, *7*, 4336.

[30] P. Munnik, P. E. de Jongh, K. P. de Jong, *Chem. Rev.* **2015**, *115*, 6687.

[31] J. Ran, J. Zhang, J. Yu, M. Jaroniec, S. Z. Qiao, *Chem. Soc. Rev.* **2014**, *43*, 7787.

[32] T. Kawawaki, Y. Mori, K. Wakamatsu, S. Ozaki, M. Kawachi, S. Hossain, Y. Negishi, *J. Mater. Chem. A* **2020**, *8*, 16081.

[33] K. Maeda, *ACS Catal.* **2013**, *3*, 1486.

[34] J. Yang, D. Wang, H. Han, C. Li, *Acc. Chem. Res.* **2013**, *46*, 1900.

[35] N. Sakamoto, H. Ohtsuka, T. Ikeda, K. Maeda, D. Lu, M. Kanehara, K. Teramura, T. Teranishi, K. Domen, *Nanoscale* **2009**, *1*, 106.

[36] S. M. Oh, S. B. Patil, X. Jin, S. J. Hwang, *Chemistry* **2018**, *24*, 4757.

[37] H. Hong, J. M. Lee, J. H. Yun, Y. J. Kim, S. il Kim, H. I. Shin, H. S. Ahn, S. J. Hwang, W. H. Ryu, *Sci. Adv.* **2021**, *7*, https://doi.org/10.1126/sciadv.abf2543.

[38] W. Sugimoto, H. Iwata, Y. Yasunaga, Y. Murakami, Y. Takasu, *Angew. Chem., Int. Ed.* **2003**, *42*, 4092.

[39] S. Laha, Y. Lee, F. Podjaski, D. Weber, V. Duppel, L. M. Schoop, F. Pielnhofer, C. Scheurer, K. Müller, U. Starke, K. Reuter, B. V. Lotsch, *Adv. Energy Mater.* **2019**, *9*, 1803795.

[40] J. M. Lee, E. K. Mok, S. Lee, N. S. Lee, L. Debbichi, H. Kim, S. J. Hwang, *Angew. Chem., Int. Ed.* **2016**, *55*, 8546.

[41] J. W. Roh, W. H. Shin, H.-S. Kim, S. Y. Kim, S. Kim, *Appl. Sci.* **2020**, *10*, 4127.

[42] P. A. Kempler, M. A. Gonzalez, K. M. Papadantonakis, N. S. Lewis, *ACS Energy Lett.* **2018**, *3*, 612.

[43] S. Morawiec, J. Holovský, M. J. Mendes, M. Müller, K. Ganzerová, A. Vetushka, M. Ledinský, F. Priolo, A. Fejfar, I. Crupi, *Sci. Rep.* **2016**, *6*, 22481.

[44] S. E. Braslavsky, A. M. Braun, A. E. Cassano, A. V. Emeline, M. I. Litter, L. Palmisano, V. N. Parmon, N. Serpone, *Pure Appl. Chem.* **2011**, *83*, 931.

[45] H. Kisch, D. Bahnemann, *J. Phys. Chem. Lett.* **2015**, *6*, 1907.

[46] M. Qureshi, K. Takanabe, *Chem. Mater.* **2017**, *29*, 158.

[47] K. Gottschling, G. Savasci, H. Vignolo-González, S. Schmidt, P. Mauker, T. Banerjee, P. Rovó, C. Ochsenfeld, B. V. Lotsch, *J. Am. Chem. Soc.* **2020**, *142*, 12146.

[48] B. P. Biswal, H. A. Vignolo-González, T. Banerjee, L. Grunenberg, G. Savasci, K. Gottschling, J. Nuss, C. Ochsenfeld, B. V. Lotsch, *J. Am. Chem. Soc.* **2019**, *141*, 11082.

[49] Y. K. Jo, J. M. Lee, S. Son, S. Hwang, *J. Photochem. Photobiol., C* **2019**, *40*, 150.

[50] J. Lim, J. M. Lee, C. Kim, S.-J. Hwang, J. Lee, W. Choi, *Environ. Sci.: Nano* **2019**, *6*, 2084.

[51] G. Chen, D. Li, F. Li, Y. Fan, H. Zhao, Y. Luo, R. Yu, Q. Meng, *Appl. Catal., A* **2012**, *443–444*, 138.

[52] K. Fukuda, T. Saida, J. Sato, M. Yonezawa, Y. Takasu, W. Sugimoto, *Inorg. Chem.* **2010**, *49*, 4391.

[53] R. Abe, K. Sayama, H. Sugihara, *J. Phys. Chem. B* **2005**, *109*, 16052.

[54] Y. Fujioka, J. Frantti, A. M. Asiri, A. Y. Obaid, H. Jiang, R. M. Nieminen, *J. Phys. Chem. C* **2012**, *116*, 17029.

[55] Y. Fujioka, J. Frantti, R. M. Nieminen, A. M. Asiri, *J. Phys. Chem. C* **2013**, *117*, 7506.

[56] K. Persson, *The Materials Project. Materials Data on RuO2 by Materials Project*, https://doi.org/10.17188/1307989 (accessed: September 2022).

[57] A. Kim, C. Sanchez, G. Patriarche, O. Ersen, S. Moldovan, A. Wisnet, C. Sassoye, D. P. Debecker, *Catal. Sci. Technol.* **2016**, *6*, 8117.

[58] B. Zhang, C. Zhang, H. He, Y. Yu, L. Wang, J. Zhang, *Chem. Mater.* **2010**, *22*, 4056.

[59] P. Praus, L. Svoboda, R. Dvorský, M. Reli, M. Kormunda, P. Mančík, *Ceram. Int.* **2017**, *43*, 13581.

[60] J. M. Lee, J. L. Gunjakar, Y. Ham, I. Y. Kim, K. Domen, S.-J. Hwang, *Chemistry* **2014**, *20*, 17004.

[61] R. Y. Parapat, O. H. I. Saputra, A. P. Ang, M. Schwarze, R. Schomäcker, *RSC Adv.* **2014**, *4*, 50955.

[62] S. L. Hemmingson, C. T. Campbell, *ACS Nano* **2017**, *11*, 1196.

[63] P. Wang, C. Jia, Y. Huang, X. Duan, *Matter* **2021**, *4*, 552.

[64] R. Dvorský, J. Trojková, P. Praus, J. Luňáček, *Mater. Res. Bull.* **2013**, *48*, 2286.

[65] D. J. Morgan, *Surf. Interface Anal.* **2015**, *47*, 1072.

[66] D.-S. Ko, W.-J. Lee, S. Sul, C. Jung, D.-J. Yun, H.-G. Kim, W.-J. Son, J. G. Chung, D. W. Jung, S. Y. Kim, J. Kim, W. Lee, C. Kwak, J. K. Shin, J.-H. Kim, J. W. Roh, *NPG Asia Mater.* **2018**, *10*, 266.

[67] J. S. de Almeida, R. Ahuja, *Phys. Rev. B* **2006**, *73*, 165102.

[68] F. El-Tantawy, A. A. Al-Ghamdi, A. A. Al-Ghamdi, Y. A. Al-Turki, A. Alshahrie, F. Al-Hazmi, O. A. Al-Hartomy, *J. Mater. Sci.: Mater. Electron.* **2017**, *28*, 52.

[69] Q. Gu, Z. Gao, S. Yu, C. Xue, *Adv. Mater. Interfaces* **2016**, *3*, 1500631.

[70] J. Yang, H. Yan, X. Zong, F. Wen, M. Liu, C. Li, *Philos. Trans. R. Soc., A* **2013**, *371*, 20110430.

[71] G. Zhao, X. Xu, *Nanoscale* **2021**, *13*, 10649.

[72] Z. Wang, T. Hisatomi, R. Li, K. Sayama, G. Liu, K. Domen, C. Li, L. Wang, *Joule* **2021**, *5*, 344.

[73] B. Liu, K. Nakata, X. Zhao, T. Ochiai, T. Murakami, A. Fujishima, *J. Phys. Chem. C* **2011**, *115*, 16037.

[74] B. Liu, X. Zhao, C. Terashima, A. Fujishima, K. Nakata, *Phys. Chem. Chem. Phys.* **2014**, *16*, 8751.

[75] K. Takanabe, *ACS Catal.* **2017**, *7*, 8006.

[76] A. Lewandowska-Andralojc, D. E. Polyansky, *J. Phys. Chem. A* **2013**, *117*, 10311.

[77] B. Limburg, E. Bouwman, S. Bonnet, *ACS Catal.* **2016**, *6*, 5273.

[78] M. T. Uddin, Y. Nicolas, C. Olivier, T. Toupance, M. M. Müller, H.-J. Kleebe, K. Rachut, J. Ziegler, A. Klein, W. Jaegermann, *J. Phys. Chem. C* **2013**, *117*, 22098.

[79] Y. Hermans, A. Klein, K. Ellmer, R. van de Krol, T. Toupance, W. Jaegermann, *J. Phys. Chem. C* **2018**, *122*, 20861.

[80] L. Li, P. A. Salvador, G. S. Rohrer, *Nanoscale* **2014**, *6*, 24.